Investigation on the mechanisms of plasmon-mediated photocatalysis: synergistic contribution of near-field and charge transfer effects

Zelio Fusco, Kylie Catchpole, Fiona J. Beck*

School of Engineering, College of Engineering and Computer Science, Australian National University, Acton, ACT 2601, Australia

Supplementary Information

Materials and Methods

Sample preparation. Disordered Au nanoparticles arrays were prepared using a Temescal BJD-2000 electron-beam thermal evaporator. Thin layers of gold with thicknesses of 2.5, 5 and 8 nm were evaporated at a rate of 0.5 Å/s onto clean quartz substrates with subsequent annealing at different temperatures (270, 300 and 500 °C) in inert (N_2) atmosphere to guarantee the formation on segregated nanoislands. *Morphological characterization.* The morphology of the resultant structures was investigated using a field emission scanning electron microscope FEI Verios operating at 3 kV. *Optical characterization.* Transmittance (T) and reflectance (R) spectra were recorded using a PerkinElmer Lambda 1050 UV-Vis-NIR spectrophotometer with an integrated sphere. The absorbance A was then obtained as A=100-R-T. *Optical simulations.* The electrodynamic behaviour of the single Au sphere was investigated through the finite element method using the radiofrequency module in the commercial software COMSOL Multiphysics 5.6. *SERS measurements.* The substrates were immersed overnight in a 5 ppm solution of methylene blue in water to guarantee the binding on the gold nanostructures[1]. The samples were then rinsed in water to remove the excess of MB and dried in air before the spectroscopic measurements. The Raman spectra were captured using a Renishaw InVia Reflex spectrometer equipped with a 533, 633 and 785 nm lasers and a 1200 l/mm grating. All the measurements were performed at room temperature, with an integration time of 1s and two accumulations for noise reduction. *Ab-initio* simulations. We used the atomic simulator environment (ASE) to build up the Au_{55}+MB model and we performed the calculations using the free GPAW package[2], which uses the projector augmented-wave (PAW) method. More details in the following page. Specifically, we use the real-time time-domain density functional theory (RT-TDDFT) implementation based on the linear combination of atomic orbitals (LCAO) representation for the wave functions[3, 4]. Default double-ζ polarized basis sets were used. The orbital-dependent GLLBSC density functional was used to improve the description of the d-band in gold. A Fermi-Dirac smearing of 0.05 was used to facilitate the convergence. The hot carrier energy distribution and the transition contribution maps were evaluated following the works of Rossi et al[3-6]. In this approach, we analyse the plasmon formation and hot-carrier generation in terms of the Kohn-Sham electron-hole transition contributions. The Kohn-Sham decomposition of the frequency-space density matrix, $\delta\rho_{ia}(t)$, in the basis of created hole (i) and electron (a) states is used to analyse electronic excitations and can be visualized at any time-step. The TCM is constructed starting from the transition probability element, $P_{ia}(t)$, which is given by $P_{ia}(t)=|\delta\rho_{ia}(t)$ / (f*i*-

f*a*)$^{0.5}$|^2, where fi and fa are the ground-state occupations of KS states *i* and *a*, respectively. By interpreting the occupied KS states as electrons and unoccupied KS states as holes, each matrix element stemming from transitions, whose eigenvalue differences are equal to the frequencies of the laser pulse P*ia*(t), is interpreted as the probability of the electron *i* being in state *a* at time t. By vertically summing all the transitions over the occupied (i) energies in the TCM is possible to obtain the hot-hole probability distribution (indicated by the blue arrows in Figure 6c-d), while the horizontal sum leads to the hot-electron probability distribution (indicated by the red arrows in Figure 6c-d).

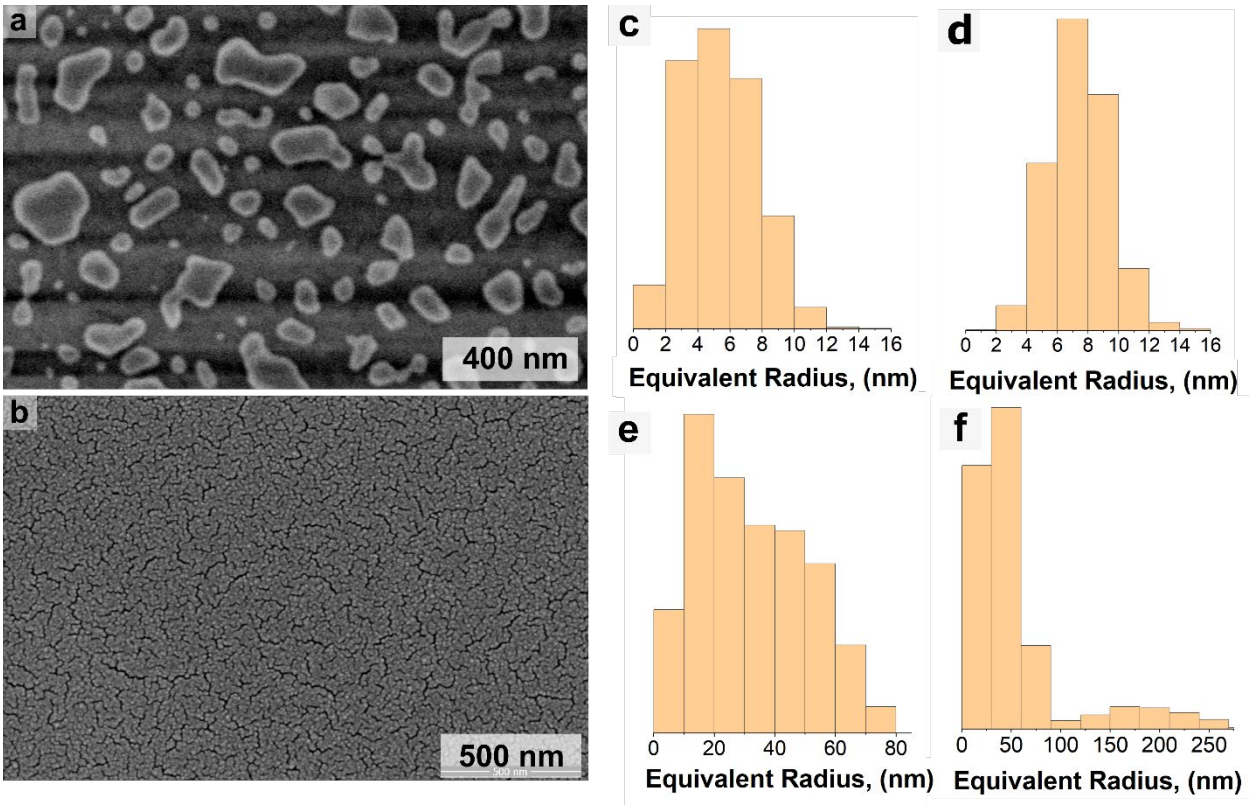

Figure S1. a-b) Top view scanning electron micrographs (SEM) of the disordered Au nanoparticles arrays with average particle size of ~65 nm and of an Au film with 15 nm of thickness. **c-f)** Histograms of the equivalent NP radius distribution for the 5 nm, 8 nm, 32 nm and 65 nm, respectively.

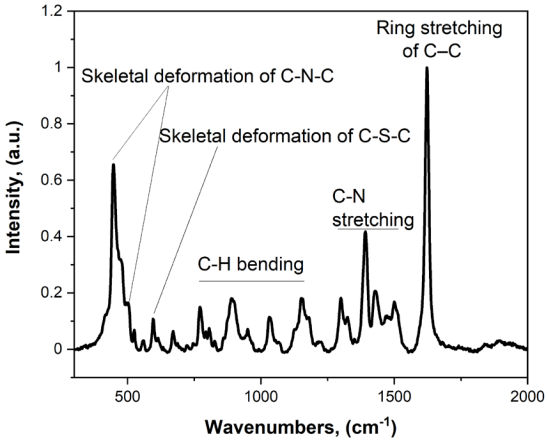

Table S1

Peak (cm^{-1})	Band Assignment	Ref.
446	C-N-C skeletal deformation	7
501	C-N-C skeletal deformation	7
601	C-S-C skeletal deformation	8
772	C-H in-plane bending	7
1390	C-N symmetric stretching	9
1426	C-N asymmetric stretching	8
1434	C-N asymmetric stretching	7
1622	C-C ring stretching	8

Figure S2. SERS spectra of MB on the 5 nm disordered Au nanoparticles array and band assignment (**Table S1**).

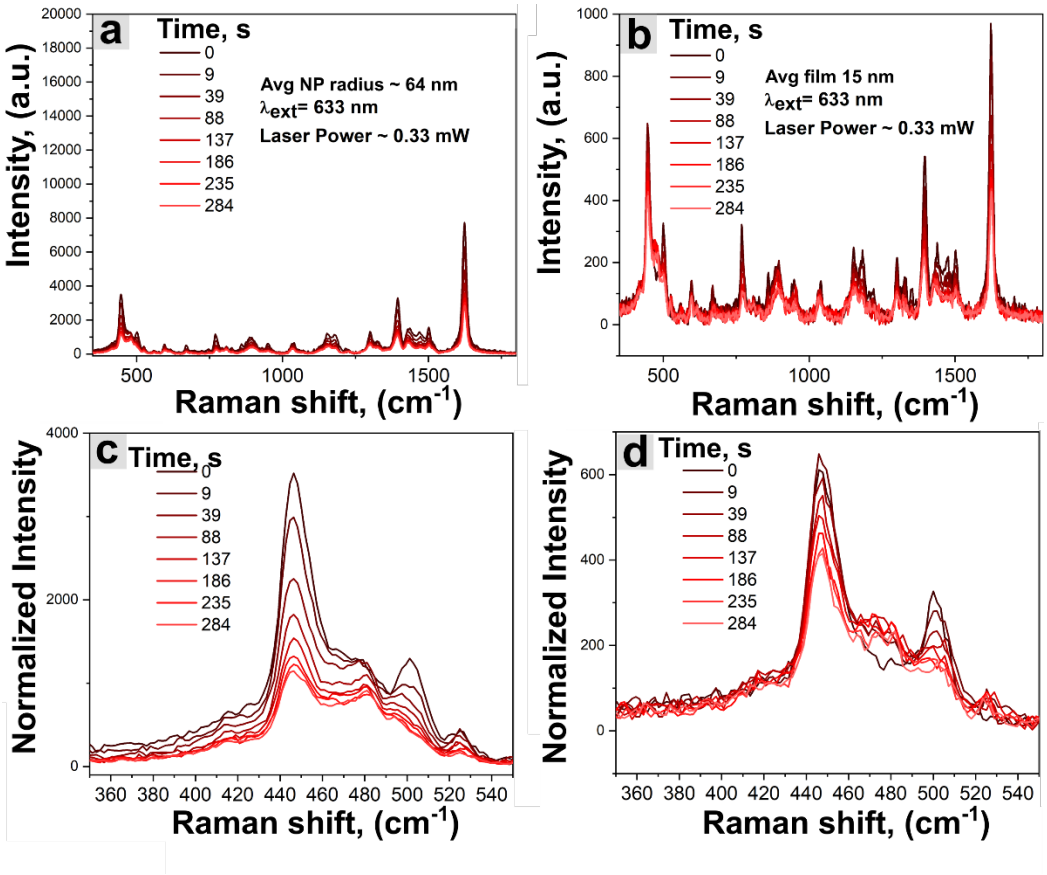

Figure S3. a,b) Temporal evolution of the SERS spectra of MB on the 65 nm Au nanoparticles arrays and the 15 nm Au film, respectively. **c,d)** Enlarged view (in the Raman shift range 350 – 560 cm-1) for the same samples in **a,b** showing an increase of the product peak with time.

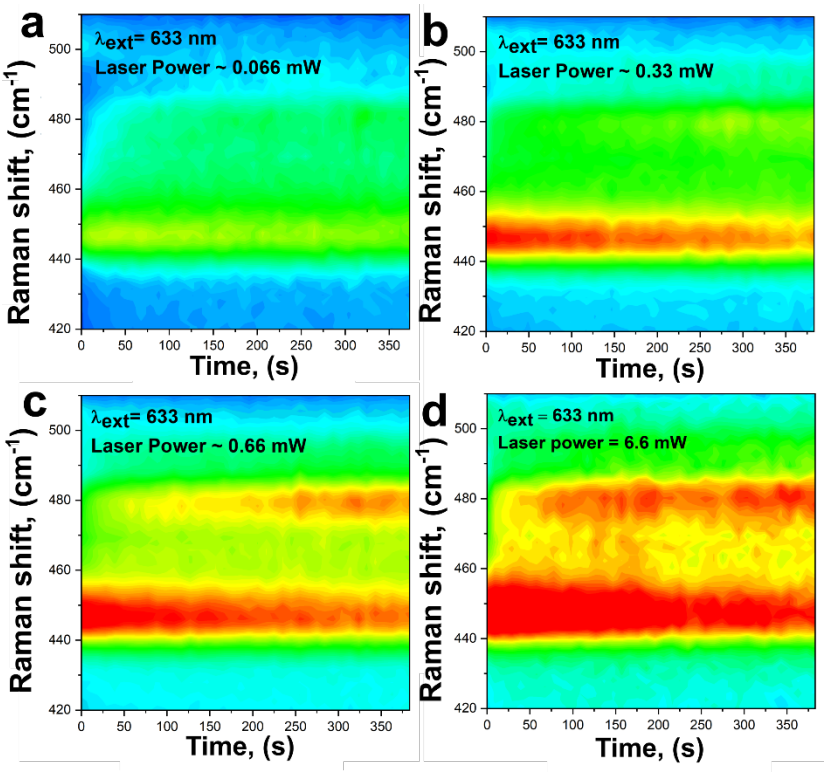

Figure S4. a-d) Time evolution of the SERS spectra (normalized) for the 5 nm Au NP array under a 633 excitation wavelength with increasing laser powers, ranging from 0.066 mW to 6.6 mW.

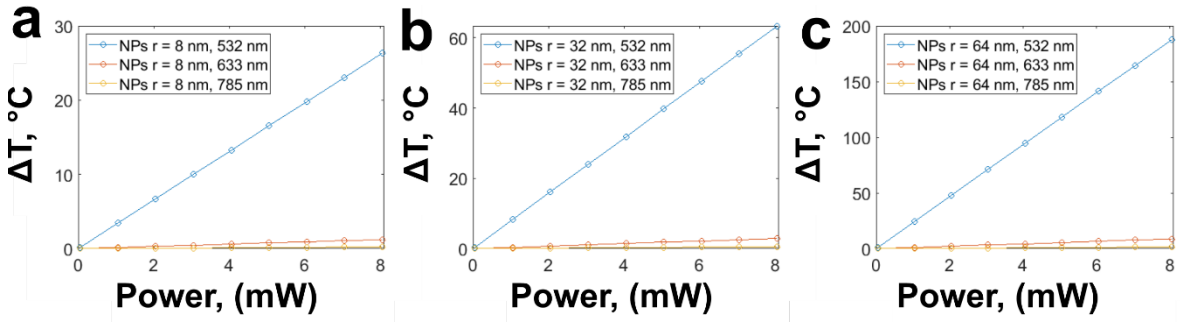

Figure S5. a-c) Computed temperature increase as a function of the laser power for a 8, 32, and 64 nm NP arrays at different illumination wavelengths, respectively.

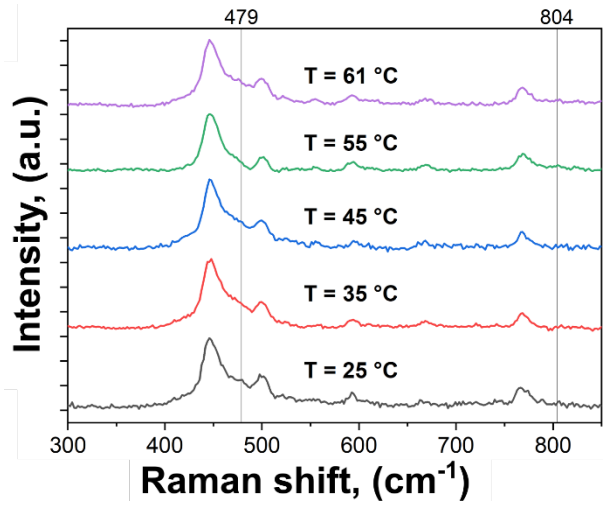

Figure S6. Raman spectra on MB powder taken at different temperatures with an excitation wavelength of 633 nm.

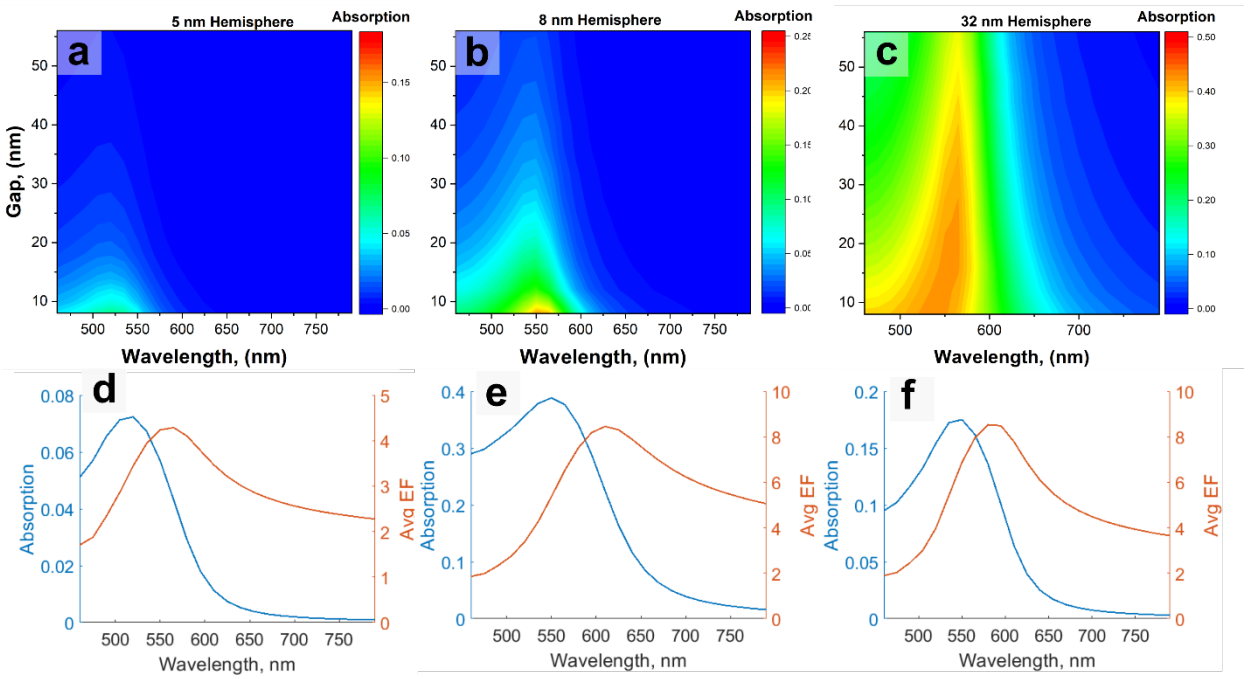

Figure S7. a-c) Colormaps of the computed absorption for the 5 nm, 8 nm and 32 nm Au hemispheres, respectively, on glass as a function of the wavelength and interparticle separation. **d-f)** Representation of the near- to far-field shift. Overlay of the computed absorption and averaged EF evaluated at a gap = 8 nm for the 5 nm ad 8 nm Au hemispheres, and gap = 28 nm for the 32 nm Au hemispheres. The plot indicates that a shift between the absorption profile and the averaged EF is always present for all the considered NP size and at all separations. This discrepancy has been explained by using a damped harmonic oscillator model for the metal conduction electrons and the mismatch was attributed to radiative and nonradiative damping in the nanostructure[10].

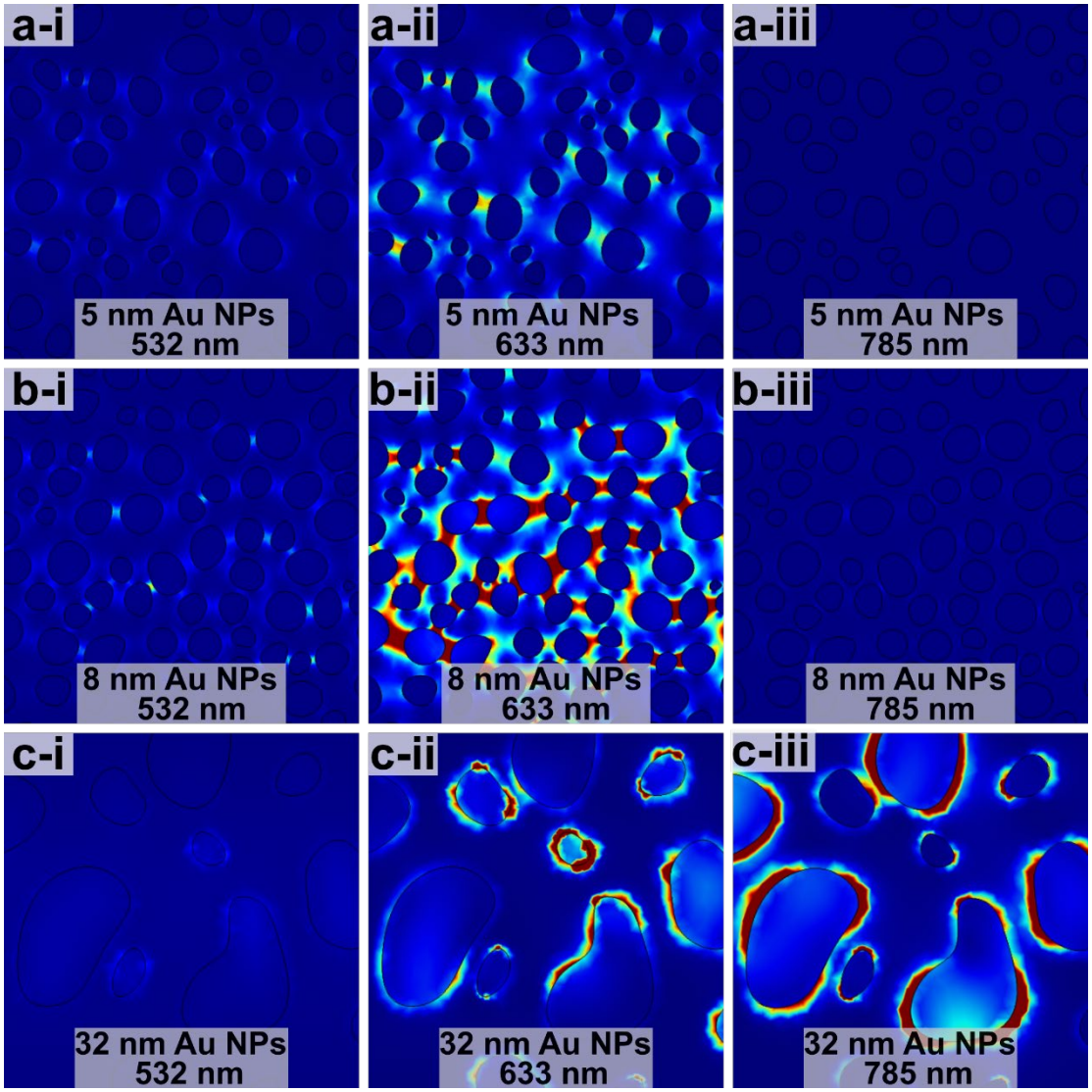

Figure S8. c-e) Spatial distributions of the $\mathbf{(E/E0)^2}$ for Au nanoparticles of different averaged dimension –5 nm, 8 nm and 32 nm, respectively, at the three illumination wavelengths considered in the main text.

The simulations of the real Au nanoparticles array were performed in COMSOL by a setting a two-step model to better approximate the behaviour of the infinitely thick substrate and to consider the proper background field to which the Au nanoparticle arrays are subjected in a not homogenous media (layered structure)[11-13]. When a scatterer is placed on a substrate, the background field becomes a superposition of the incident plane wave and its reflected and transmitted component from the substrate. This field is calculated in the first step with a full-field formulation by setting a two-layers system, comprising of glass (n=1.45) and air (n=1). Floquet periodicity is imposed on the side boundaries to guarantee the semi-infinite layers in the *xy*-plane. A plane wave is injected orthogonally to the substrate by a port located at the top boundary of the domain to excite the system. The solution of this computation is then fed as background field for the second step of the simulation (scattered-field), where the Au nanoparticles arrays are added on top of the substrate and perfectly matched layers are used to avoid reflections and absorb the

electromagnetic waves. The spatial distributions of the Au nanoparticles were taken from the binarization of the respective SEM images and their thickness was set to 10 nm.

A widely used parameter to estimate the efficiency of a SERS substrate from experimental measurements is the enhancement factor, defined as[14]:

$$EF = \frac{I_{SERS}/N_{SERS}}{I_{Raman}/N_{vol}}$$

where I_{SERS} and I_{Raman} are the SERS and Raman intensity, respectively; while N_{SERS} is the number of molecules excited in the SERS experiment and N_{vol} is the number of molecule excited in the Raman measurement, taken under the same conditions. The number of adsorbed MB molecules illuminated by the laser on the Au surface can be computed as $N_{SERS} = N_d A_{laser} A_N/\sigma$, where N_d is the numerical density of Au NPs, A_{laser} is the spot size of the laser and A_N/σ is the footprint area of the Au NPs normalized for the surface area occupied from a MB molecule.[15] The number of molecules excited within normal Raman experiments can be evaluated as $N_{vol} = \frac{N_A A_{laser} h \rho}{MW}$, where N_A is the Avogadro number, h is the penetration depth of the laser and ρ, MW are the density and molecular weight of MB, respectively. By using this procedure, the computed EFs for our disordered Au NPs arrays with average radius of 5 to 32 nm all have the same magnitude and range from ~1.5 – 6 x 10^7. The EFs have been computed from the peaks at 1622 cm^{-1}, 446 cm^{-1} and 1392 cm^{-1}. The experimentally observed trend may be due to fluctuations of the field intensity density due to the higher nanoparticle density of smaller Au NPs arrays and/or fluctuation in the number of MB molecules involved in the SERS process (formation of a non-perfect monolayer on the Au NPs surface). In addition, this procedure does not consider possible chemical enhancement effects that have been shown to contribute by a factor of 10-100 to the overall SERS enhancement[16, 17].

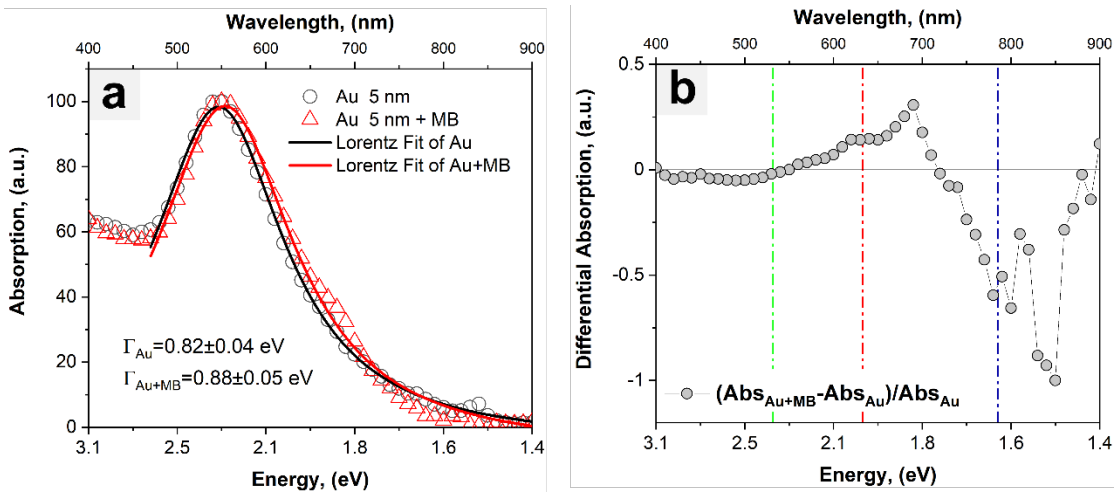

Figure S9. a) Normalized UV-Vis absorption spectra as a function of the energy for the 5 nm Au nanoparticle array and the same after 5 ppm MB functionalization (circles and triangles, respectively) fitted by a Lorentian function (solid black and red lines). Labelled are the computed full-width half maximum (Γ) of the two systems. As the plasmon resonance depends on the dielectric function of the surrounding environment, a broadening of the resonance provides indications about molecules that are chemically bound to the metal nanoparticles[18]. The broadening of the peak is attributed to an increase in the chemical interface dampening (CID), one of the possible plasmon decay channels[19]. **b)** Differential absorption (DA), evaluated as a difference between the UV-Vis absorption spectra of the functionalized system (Au+MB) and the bare 5 nm Au nanoparticle array, normalized to the latter, $DA = (Abs_{Au+MB} - Abs_{Au})/Abs_{Au}$. The DA spectrum provides a useful way of revealing changes in optical properties due binding events or reactions[20-22]. The vertical dashed lines represent the lasers excitation wavelengths. The DA spectra can be used to enhance small changes in the optical properties of the functionalized system and provides information on the interaction between MB and the Au nanoparticle array. As the absorption spectrum is in direct correlation with the optical density of the states[23], DA provides a way to visualise and analyse the relative contribution of the interactions. The DA spectrum is relatively flat for wavelength <550 nm, meaning that in this region the spectra is dominated by the plasmon resonance of the Au nanoparticles. A positive band appears between ~600 nm and ~700 nm which is due to the main absorption of MB, coherently with its HOMO-LUMO of ~1.86 eV. At lower energies (<1.8 eV), the DA spectrum shows a wide negative band with a relative minimum overlapping the 785 nm excitation wavelength. We attribute this difference to the presence of hybridized Au-MB electronic states.

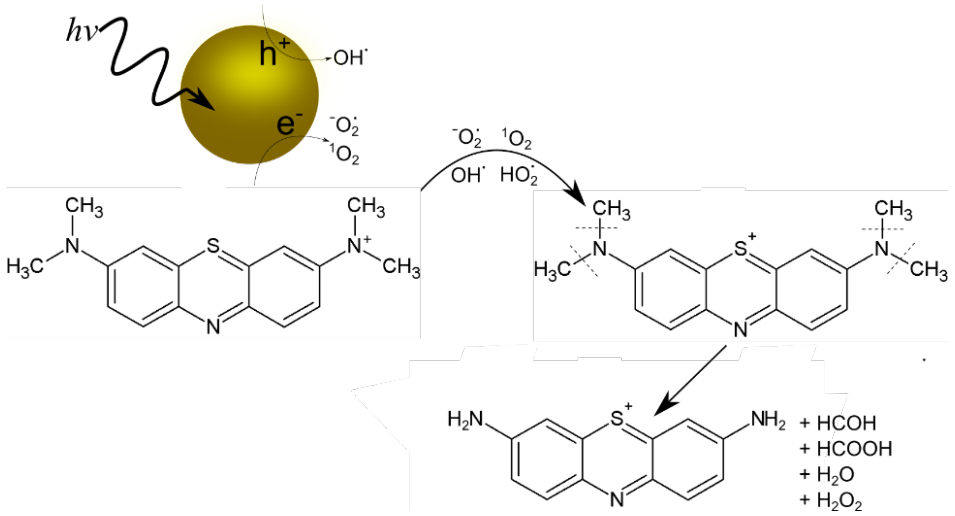

Figure S10. Schematic of the N-demethylation reaction mechanism. Not in scale, is shown the generation of transient radical species (1O2, ·O2-, OH·) from photogenerated hot carriers arising from the nonradiative decay of the plasmon, and their probable effect in the conversion of methylene blue.

Upon non-radiative plasmon decay, hot electrons and hot holes are generated within the Au NPs, as described by equation (1)

$$Au + h\upsilon \rightarrow e^- + h^+ \quad (1)$$

Hot electrons with suitable energy and momentum can excite MB to its singlet state. Upon decay, MB transfer its energy to oxygen species in the local environment producing singlet oxygen (equation (2)). Alternatively, the hot electrons can transfer their energy directly to molecular oxygen to generate superoxide radicals (equation (3)).

$$e^- + MB + O_2 \rightarrow MB^* + O_2 \rightarrow MB + {}^1O_2 \quad (2)$$

$$e^- + O_2 \rightarrow {}^{\cdot}O_2^- \quad (3)$$

Simultaneously, hot holes produced by the plasmon decay can either directly oxidize MB (equation 4) or can oxidise water molecules to form reactive ·OH and $HO_2^{\cdot}$ species[24](equation (5) and (6)).

$$h^+ + MB \rightarrow MB^+ \quad (4)$$

$$h^+ + H_2O \rightarrow OH^{\cdot} + H^+ \quad (5)$$

$$H^+ + {}^{\cdot}O_2^- \rightarrow HO_2^{\cdot} \quad (6)$$

Finally, all these transient radical species can participate in the cleavage of the C-N bond (N-demethylation reaction) and thus the degradation of methylene blue (equation (7)).

$${}^1O_2, {}^{\cdot}O_2^-, OH^{\cdot}, HO_2^{\cdot} + MB \rightarrow \text{degradation of MB}” \quad (7)$$

References

1. Fazio, B.; D'Andrea, C.; Bonaccorso, F.; Irrera, A.; Calogero, G.; Vasi, C.; Gucciardi, P. G.; Allegrini, M.; Toma, A.; Chiappe, D.; Martella, C.; Buatier de Mongeot, F., Re-radiation Enhancement in Polarized Surface-Enhanced Resonant Raman Scattering of Randomly Oriented Molecules on Self-Organized Gold Nanowires. *ACS Nano* **2011,** *5* (7), 5945-5956.
2. Enkovaara, J.; Rostgaard, C.; Mortensen, J. J.; Chen, J.; Dułak, M.; Ferrighi, L.; Gavnholt, J.; Glinsvad, C.; Haikola, V.; Hansen, H. A.; Kristoffersen, H. H.; Kuisma, M.; Larsen, A. H.; Lehtovaara, L.; Ljungberg, M.; Lopez-Acevedo, O.; Moses, P. G.; Ojanen, J.; Olsen, T.; Petzold, V.; Romero, N. A.; Stausholm-Møller, J.; Strange, M.; Tritsaris, G. A.; Vanin, M.; Walter, M.; Hammer, B.; Häkkinen, H.; Madsen, G. K. H.; Nieminen, R. M.; Nørskov, J. K.; Puska, M.; Rantala, T. T.; Schiøtz, J.; Thygesen, K. S.; Jacobsen, K. W., Electronic structure calculations with GPAW: a real-space implementation of the projector augmented-wave method. *Journal of Physics: Condensed Matter* **2010,** *22* (25), 253202.
3. Rossi, T. P.; Kuisma, M.; Puska, M. J.; Nieminen, R. M.; Erhart, P., Kohn-Sham Decomposition in Real-Time Time-Dependent Density-Functional Theory: An Efficient Tool for Analyzing Plasmonic Excitations. *J Chem Theory Comput* **2017,** *13* (10), 4779-4790.
4. Rossi, T. P.; Erhart, P.; Kuisma, M., Hot-Carrier Generation in Plasmonic Nanoparticles: The Importance of Atomic Structure. *ACS Nano* **2020,** *14* (8), 9963-9971.
5. Kumar, P. V.; Rossi, T. P.; Kuisma, M.; Erhart, P.; Norris, D. J., Direct hot-carrier transfer in plasmonic catalysis. *Faraday Discuss* **2019,** *214*, 189-197.
6. Kumar, P. V.; Rossi, T. P.; Marti-Dafcik, D.; Reichmuth, D.; Kuisma, M.; Erhart, P.; Puska, M. J.; Norris, D. J., Plasmon-Induced Direct Hot-Carrier Transfer at Metal-Acceptor Interfaces. *ACS Nano* **2019,** *13* (3), 3188-3195.
7. Xiao, G.-N.; Man, S.-Q., Surface-enhanced Raman scattering of methylene blue adsorbed on cap-shaped silver nanoparticles. *Chemical Physics Letters* **2007,** *447* (4), 305-309.
8. Ruan, C.; Wang, W.; Gu, B., Single-molecule detection of thionine on aggregated gold nanoparticles by surface enhanced Raman scattering. *Journal of Raman Spectroscopy* **2007,** *38* (5), 568-573.
9. Naujok, R. R.; Duevel, R. V.; Corn, R. M., Fluorescence and Fourier Transform surface-enhanced Raman scattering measurements of methylene blue adsorbed onto a sulfur-modified gold electrode. *Langmuir* **1993,** *9* (7), 1771-1774.
10. Zuloaga, J.; Nordlander, P., On the Energy Shift between Near-Field and Far-Field Peak Intensities in Localized Plasmon Systems. *Nano Letters* **2011,** *11* (3), 1280-1283.
11. Rose, A.; Hoang, T. B.; McGuire, F.; Mock, J. J.; Ciracì, C.; Smith, D. R.; Mikkelsen, M. H., Control of Radiative Processes Using Tunable Plasmonic Nanopatch Antennas. *Nano Letters* **2014,** *14* (8), 4797-4802.
12. Li, G.-C.; Zhang, Q.; Maier, S. A.; Lei, D., Plasmonic particle-on-film nanocavities: a versatile platform for plasmon-enhanced spectroscopy and photochemistry. *Nanophotonics* **2018,** *7* (12), 1865-1889.
13. Hill, R. T.; Mock, J. J.; Urzhumov, Y.; Sebba, D. S.; Oldenburg, S. J.; Chen, S.-Y.; Lazarides, A. A.; Chilkoti, A.; Smith, D. R., Leveraging Nanoscale Plasmonic Modes to Achieve Reproducible Enhancement of Light. *Nano Letters* **2010,** *10* (10), 4150-4154.
14. Stiles, P. L.; Dieringer, J. A.; Shah, N. C.; Van Duyne, R. P., Surface-enhanced Raman spectroscopy. *Annu Rev Anal Chem (Palo Alto Calif)* **2008,** *1*, 601-26.
15. Jia, H.; Bai, X.; Li, N.; Yu, L.; Zheng, L., Siloxane surfactant induced self-assembly of gold nanoparticles and their application to SERS. *CrystEngComm* **2011,** *13* (20), 6179-6184.
16. Kneipp, K.; Kneipp, H.; Itzkan, I.; Dasari, R. R.; Feld, M. S., Ultrasensitive Chemical Analysis by Raman Spectroscopy. *Chemical Reviews* **1999,** *99* (10), 2957-2976.

17. Gieseking, R. L.; Ratner, M. A.; Schatz, G. C., Review of Plasmon-Induced Hot-Electron Dynamics and Related SERS Chemical Effects. In *Frontiers of Plasmon Enhanced Spectroscopy Volume 1*, American Chemical Society: 2016; Vol. 1245, pp 1-22.
18. Szekrényes, D. P.; Kovács, D.; Zolnai, Z.; Deák, A., Chemical Interface Damping as an Indicator for Hexadecyltrimethylammonium Bromide Replacement by Short-Chain Thiols on Gold Nanorods. *The Journal of Physical Chemistry C* **2020,** *124* (36), 19736-19742.
19. Foerster, B.; Joplin, A.; Kaefer, K.; Celiksoy, S.; Link, S.; Sönnichsen, C., Chemical Interface Damping Depends on Electrons Reaching the Surface. *ACS Nano* **2017,** *11* (3), 2886-2893.
20. Yin, C.; Meng, F.; Meng, Y.; Chen, G.-H., Differential ultraviolet–visible absorbance spectra for characterizing metal ions binding onto extracellular polymeric substances in different mixed microbial cultures. *Chemosphere* **2016,** *159*, 267-274.
21. Huang, S.; Gan, W.; Yan, M.; Zhang, X.; Zhong, Y.; Yang, X., Differential UV–vis absorbance can characterize the reaction of organic matter with ClO2. *Water Research* **2018,** *139*, 442-449.
22. Umeyama, T.; Baek, J.; Sato, Y.; Suenaga, K.; Abou-Chahine, F.; Tkachenko, N. V.; Lemmetyinen, H.; Imahori, H., Molecular interactions on single-walled carbon nanotubes revealed by high-resolution transmission microscopy. *Nature Communications* **2015,** *6* (1), 7732.
23. Cardona, M. In *Optical Properties and Electronic Density of States * 1*, 2010.
24. Khan, I.; Saeed, K.; Zekker, I.; Zhang, B.; Hendi, A. H.; Ahmad, A.; Ahmad, S.; Zada, N.; Ahmad, H.; Shah, L. A.; Shah, T.; Khan, I., Review on Methylene Blue: Its Properties, Uses, Toxicity and Photodegradation. *Water* **2022,** *14* (2).